The near-edge structure in energy-loss spectroscopy: many-electron and magnetic effects in transition metal nitrides and carbides

2000 J. Phys.: Condens. Matter 12 729

(http://iopscience.iop.org/0953-8984/12/5/319)

J. Phys.: Condens. Matter **12** (2000) 729–750. Printed in the UK PII: S0953-8984(00)09060-3

The near-edge structure in energy-loss spectroscopy: many-electron and magnetic effects in transition metal nitrides and carbides

A T Paxton†, M van Schilfgaarde‡, M MacKenzie§ and A J Craven§

† Atomistic Simulation Group, Department of Pure and Applied Physics, Queen's University, Belfast BT7 1NN, UK
‡ Sandia National Laboratories, Livermore, CA 94551, USA
§ Department of Physics and Astronomy, University of Glasgow, Glasgow G12 8QQ, UK

Received 28 October 1999

Abstract. We investigate the ability of the local density approximation (LDA) in density functional theory to predict the near-edge structure in electron energy-loss spectroscopy in the dipole approximation. We include screening of the core hole within the LDA using Slater's transition state theory. We find that anion K-edge threshold energies are systematically overestimated by 4.22 ± 0.44 eV in twelve transition metal carbides and nitrides in the rock-salt (B1) structure. When we apply this 'universal' many-electron correction to energy-loss spectra calculated within the transition state approximation to LDA, we find quantitative agreement with experiment to within one or two eV for TiC, TiN and VN. We compare our calculations to a simpler approach using a projected Mulliken density which honours the dipole selection rule, in place of the dipole matrix element itself. We find remarkably close agreement between these two approaches. Finally, we show an anomaly in the near-edge structure in CrN to be due to magnetic structure. In particular, we find that the N K edge in fact probes the magnetic moments and alignments of the Cr sublattice.

1. Introduction

The near-edge and extended fine structure in electron energy-loss spectroscopy (EELS) and x-ray absorption spectroscopy (XAS) contain a wealth of information about the electronic and atomic structure of solids. Our intention in this paper is to explore ways of calculating the near-edge structure in EELS and XAS. This has been done in the past by many authors (for reviews, see references [1–3] and references therein) but a number of important questions remain to be addressed. We will investigate firstly the accuracy of the threshold energy so that we can predict the energy loss in absolute terms. Secondly we will invoke a comparison between explicit calculation of the dipole matrix element and the intuitively simpler task of evaluating the local density of states projected onto a suitable local orbital. Finally we describe our discovery of how magnetism in CrN affects the measured spectrum and we propose a novel application of EELS and XANES, namely to probe the magnetic structure of alloys and its temperature dependence.

As explained by Lee and Pendry [4], the oscillatory extended fine structure (typically 20 eV or more above the threshold, or *edge*, for core-level excitations) can be interpreted as arising from the first few shells of neighbours to the excited atom. On the other hand the EELS and XAS near-edge structures (ELNES and XANES) provide information about the bandstructure or local density of states. The explanation is briefly as follows. When a

0953-8984/00/050729+22$30.00

fast-electron beam or x-ray irradiation is inelastically scattered by an atom at the origin, in a single-particle picture a core electron is said to be excited into an unoccupied state. This state can be represented mathematically as proportional to an 'outgoing partial wave'—a solid Neumann or Hankel function $h_\ell(kr)Y_{\ell m}(\hat{\boldsymbol{r}})$—which is a solution of Schrödinger's equation in a spherical potential centred at the origin. Selection rules demand that the angular momentum ℓ of the final state is that of the core state plus or minus one. The near-edge structure in a free atom *in vacuo* or in dilute gas can then be calculated and, at least in the case of the K edge, turns out to be a monotonically decaying intensity as a function of energy above the excitation edge [5, 6]. In a solid the outgoing wave interferes with 'incoming waves'—Bessel function solutions $j_\ell(kr)Y_{\ell m}(\hat{\boldsymbol{r}})$ of Schrödinger's equation in the potential centred around the other atomic sites in the crystal. One then may make a hierarchy of approximations to calculate the structure superimposed upon the atomic background. Lee and Pendry show that the extended fine structure may be calculated in a single-scattering approximation (which means including interference of the outgoing wave with just one backscattered wave from each shell of neighbours); however, the near-edge structure can be predicted only if multiple-scattering is included in which the outgoing wave scatters a number of times before returning to the central site at the origin. The multiple-scattering calculation amounts essentially to a cluster electronic structure calculation in the approximation of a muffin-tin potential and usually an increasing number of neighbour shells are included as one builds up the structure of the absorption spectrum. This approach allows valuable insight to be gained into the contribution that successively more distant neighbour shells make to features in the near-edge and extended fine structure. This is reminiscent of the method of moments in constructing the density of states in tight-binding theory [7]. The drawback is that shape approximations are imposed on the crystal potential, which is usually not self-consistent [8]; computation of all important scattering paths becomes non-trivial, and convergence may be not be achieved in all problems [9, 10]. The most recent calculations in multiple-scattering theory used a self-consistent potential, but the muffin-tin shape approximation was still necessary [3]. An alternative approach is to recognize that throughout one wanted the bandstructure, to calculate it by standard means (LAPW, LMTO, pseudopotential plane wave etc) and extract the relevant transition matrix elements. This approach was pioneered by Müller *et al* for extended fine structure [11] and recently reformulated by Muller *et al* [12]. The latter authors also used the theory to relate spectroscopic information to the electronic structure contribution to bonding in alloys and at crystal defects [13].

Because modern bandstructure methods make few or no approximations beyond the local density approximation (LDA) to density functional theory [14, 15], one is led to make quantitative comparisons between experiment and theory of the near-edge structure. In the present paper we compare the calculated threshold energies with the experimental ones for a range of transition metal carbides and nitrides with the B1 structure and make a comparison of the predicted and experimental near-edge structures for TiC, TiN, VN and CrN. These materials are interesting since they possess both functional and structural applications, particularly due to their strong bonding and stability. They also represent a suitable model series of materials since their electronic structures turn out to be well approximated in a rigid-band model.

The structure of the paper is as follows. In section 2 we give details of experimental methods and section 3 reviews the underlying theory of the near-edge structure. We describe the calculation of threshold energy in section 4. In section 5 we show calculated electronic structure; and go on to predict spectra in section 6. In section 7 we describe how EELS probes the magnetic structure of CrN, and show that there remains a complex pattern of local moments above the Néel temperature. Discussion and conclusions may be found in sections 8 and 9.

2. Experimental methods

With the exception of the value for CrN, all of our experimental thresholds have been published previously [16, 17]. In addition, all the materials used in that previous work have had their structures confirmed by powder x-ray diffraction which also showed that their lattice parameters were consistent with those given by Goldschmidt [18] for compounds close to stoichiometry. Since this work, energy-loss data for CrN were acquired in a manner similar to that used for the other nitrides [16] and edge shapes from other samples of TiN and VN have been acquired. Below, the key points are covered briefly while the details can be found in the earlier papers. The x-ray absorption data for CrN have not been reported before and the details of the method used are given below.

2.1. Materials

Only the new materials are considered here. The CrN powder was purchased from the same supplier as those used in the earlier work. It was supplied as at least 99% pure with a composition close to stoichiometry although no detailed analysis was provided. As for all these commercial materials, the particles in the powder had an oxide coating. X-ray diffraction gave a pattern which was indexed as the rock-salt structure with a lattice parameter consistent with the most stoichiometric composition given by Goldschmidt [18]. The absence of reflections from the oxide suggest that it was present as an amorphous phase.

The new TiN sample was a powder, plasma treated in N_2 gas to ensure that it was close to stoichiometry. Its x-ray diffraction pattern was consistent with this. The new VN sample was prepared and characterized by Lengauer and Ettmayer [19] as $VN_{0.991}$. Pflüger *et al* [20] show that sub-stoichiometry has no effect on the threshold energy of the C K edge in TiC but does cause changes in the edge shape that are relatively subtle for small degrees of sub-stoichiometry. Thus, while the edge shapes from these new samples are used here, the threshold energies are taken from the original work.

2.2. Electron energy-loss spectroscopy

For electron energy-loss spectroscopy, each material was lightly crushed by impact in an agate mortar and pestle. The crushed powder was dispersed in propan-2-ol and drops of the suspension were placed on a holey carbon film supported on an electron microscope grid. Such specimens provide freshly fractured thin regions of material, free of oxide and overhanging the edge of the carbon film. These small regions can be studied using an electron spectrometer attached to an electron microscope.

The electron energy-loss spectra were recorded using a GATAN 666 electron spectrometer which uses a photodiode array as the detector. This spectrometer was mounted on a VG Microscopes HB5 scanning transmission electron microscope with post-specimen lenses [21]. The HB5 was operated at 100 keV with a probe convergence half-angle of 11 mrad and a spectrometer acceptance half-angle of $\theta_{max} = 12.5$ mrad (see figure 1). The probe diameter was $\sim$1 nm and the probe current was $\sim$0.2 nA. The FWHM of the zero-loss peak was typically 0.3 to 0.4 eV. Operated in this way, the spectrometer integrates over a distribution of scattering vectors with a FWHM of $\sim$20 mrad.

The temperature dependence of the shape of the N K edge in CrN was investigated in a Philips CM20 FEG transmission electron microscope operated at 200 keV and equipped with a similar GATAN 666 electron spectrometer system. The incident probe half-angle was 6.1 mrad and the spectrometer half-angle of collection was $\theta = 5.1$ mrad. A GATAN double-tilt

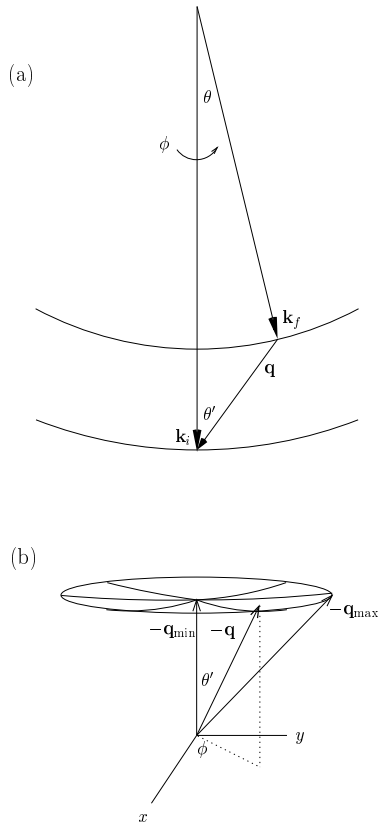

Figure 1. (a) The geometry of the inelastic scattering in wavevector space. θ and ϕ are polar and azimuthal angles subtended by the free-electron wavevector $\boldsymbol{k}_f$ of the outgoing electron beam relative to that of the incoming beam $\boldsymbol{k}_i$ which is taken along the $-z$-direction. The lower curve is a section through a Ewald sphere: the locus of all $\boldsymbol{k}$-vectors of magnitude $k = \bar{h}^{-1}\sqrt{2mE_0}$ where E_0 is the energy of the incoming electron beam (typically 100–200 keV). The upper curve represents the Ewald sphere for the outgoing beam with energy loss equal to $(\bar{h}^2/2m)(k_f^2 - k_i^2)$, typically a few hundred eV—the diagram is not to scale. θ is the half-angle subtended at the detector, its maximum value θ_{max} is typically 5–20 mrad. (b) For a given energy loss, the vector $-\boldsymbol{q}$ traces the surface of a spherical cap (a segment of the Ewald sphere of $\boldsymbol{k}_f$) with radius of curvature k_f, whose circumference is determined by the maximum half-angle θ_{max} which in turn depends on q_{max}. The shortest $\boldsymbol{q}$-vector is that for forward scattering. The diagram illustrates the integration between $\boldsymbol{q}_{\text{min}}$ and $\boldsymbol{q}_{\text{max}}$ in the text.

liquid-N-cooled Be x-ray rod and a Philips single-tilt heating rod were used. Spectra were recorded at room temperature, at -140°C and at $+260^{\circ}$C. The temperatures were measured with the thermocouples supplied with the specimen rods. No detectable change in the edge shape was observed.

In all cases, spectra were recorded from thin regions overhanging the edge of the holey carbon film using a dispersion of 0.1 eV/channel. During acquisition, the probe was scanned over an area typically 13 nm $\times$ 10 nm to prevent any radiation-induced changes. Data from areas where the spectra showed a detectable O K edge were discarded. To minimize the fixed pattern noise inherent in the photodiode detector, spectra were recorded at a number of positions on the array and subsequently aligned and summed. The spectra had the background removed and were corrected for the effects of multiple energy losses and for the broadening

due to the detection system. Details of the procedures are given in the earlier papers [16, 17].

To determine the absolute energy of an edge threshold, it is necessary to compare the position of the zero-loss peak in one spectrum with the position of the threshold in a second spectrum recorded with a voltage applied to the flight tube of the spectrometer. The voltage is chosen so that the energy of electrons which have excited the state of interest is raised to approximately that of the incident electrons. In this way the edge appears at a similar position on the diode array. Unfortunately any change in either the EHT voltage of the microscope or the prism current of the spectrometer between recording the individual spectra results in an error. This can be overcome by recording a sequence of spectra alternating between the zero-loss peak and the edge. In this way the effects of a steady drift and sudden jumps can be detected and allowed for. The values obtained in this way show consistent patterns and are in good agreement with values reported by Fink and co-workers [20, 22]. However, there are some discrepancies of $\sim$0.5 eV which are bigger than the experimental errors. These appear to arise from the fact that a much lower mean incident current is used to record the zero-loss peak than is used to record the edge in our equipment. It appears that the oxide coating on the particles causes a different level of charging of the particle for the two classes of spectra. In some way, this causes a systematic shift in the threshold energy. The effect is that the value determined at a given position is precise but can differ from the value for a different particle by more than the combined standard errors. The problem appears to be worse with the nitrides than the carbides and, in part, explains the larger errors on our values for the nitrogen thresholds (see table 1, below). In principle, the method used by Fink and co-workers [20, 22] is independent of drifts in the high-voltage supply and, *prima facie*, their values should be more accurate. Thus, where they are available, we have used them rather than our own. In some cases, their experimental values are more consistent with our calculations while, in others, the reverse is true.

Table 1. The threshold energy E_{th} (eV) at the anion K edge, calculated in the one-electron approximation (1e), from the total-energy difference (ΔSCF) and in the Slater transition state theory (TS); compared with experiment. The mean value of the one-electron error is -22.91 for the nitrides and -19.66 for the carbides. For the error in the transition state data the mean values are 4.45 for the nitrides and 3.99 for the carbides. The mean error from the TS for all carbides and nitrides is 4.22 ± 0.44. The experimental value for CrN is previously unpublished; other data are from references [16, 17] except those marked with an asterisk which are from references [20, 22] (see section 2.2).

	1e	ΔSCF	TS	Experiment	1e error	TS error
TiN	373.88	401.17	401.20	397.0 ± 0.2	-23.12	4.20
VN	374.14	401.39	401.49	$396.8 \pm 0.15^*$	-22.66	4.69
CrN	374.41	401.22	401.35	397.3 ± 0.5	-22.89	4.05
ZrN	374.23	401.56	401.56	$397.3 \pm 0.15^*$	-23.07	4.26
NbN	374.66	402.05	402.28	$397.5 \pm 0.15^*$	-22.84	4.78
HfN	374.64	402.18	402.20	397.5 ± 0.2	-22.86	4.70
TiC	261.79	285.14	285.36	$281.5 \pm 0.15^*$	-19.71	3.86
VC	262.77	285.80	285.89	$282.6 \pm 0.15^*$	-19.83	3.29
ZrC	261.60	285.32	285.61	281.4 ± 0.2	-19.80	4.21
NbC	262.98	286.18	286.23	$282.5 \pm 0.15^*$	-19.52	3.73
HfC	261.44	285.51	285.88	281.4 ± 0.2	-19.96	4.48
TaC	263.09	286.51	286.56	282.2 ± 0.2	-19.11	4.36

2.3. X-ray absorption spectroscopy

For XAS, a slurry of the CrN powder in acetone was made; this was used to form a uniform coating on a tantalum foil which was mounted on the sample holder in the beam line. No attempt was made to remove the oxide coating from the individual particles.

The XAS was carried out on the 1.1 beam line of the Synchrotron Radiation Source at the Daresbury Laboratory. The grating used had 1800 lines per mm and was operated in negative order. The Ni-coated area of the grating was used although the N K edge is just too low in energy to benefit from the reduction in the second-order radiation provided by the absorption of the Ni L edges at ∼850 eV. There was no window between the source and the sample. The absorption was measured from the total electron yield. The incident intensity, I_0, was monitored using a Keithley electrometer to measure the current to ground from a gold mesh which had been thoroughly cleaned by argon-ion bombardment. The current to ground from the specimen, I_e, was measured using a second Keithley electrometer. The absorption was taken as proportional to I_e/I_0. The energy scan was in steps of 0.5 eV between 370 and 390 eV and above 420 eV and 0.1 eV between 390 and 420 eV.

The background under the N K edge was assumed to have a similar form to that under the N K edge in an electron energy-loss spectrum, i.e., a functional form AE^{-r} where E is the energy and A and r are fitting constants. By fitting a straight line to $\ln(I_e/I_0)$ versus $\ln(E)$ in the region 320 eV to 380 eV prior to the edge, the background can be extrapolated under the edge and subtracted. Since it is difficult to determine the absolute energy of the threshold, the x-ray absorption data were shifted by 0.6 eV to align the threshold to that of the electron energy-loss data.

3. Theory

After making the dipole approximation (described below) the theories of EELS and XAS lead to similar expressions for the intensity of absorption or inelastic scattering cross section [23]. We will consider the case of EELS in which a beam of electrons in plane-wave states whose wavefunctions $\psi(\boldsymbol{r})$ are proportional to $\mathrm{e}^{\mathrm{i}\boldsymbol{k}_i\cdot\boldsymbol{r}}$ passes through a foil of material and is scattered inelastically into other plane-wave states with wavevectors $\boldsymbol{k}_f$. Thus $\boldsymbol{k}_i$ and $\boldsymbol{k}_f$ are initial and final wavevectors of the electron beam, $\hbar\boldsymbol{q} = \hbar(\boldsymbol{k}_i - \boldsymbol{k}_f)$ being the momentum transferred to the scatterer. For scattering from an isolated atom *in vacuo* under these conditions one can write down an expression for the cross section σ_f [24] for scattering into a particular final state [25]:

$$\sigma_f = \left(\frac{2me^2}{\hbar^2}\right)^2 \frac{k_f}{k_i} \int \mathrm{d}\Omega \, \frac{\left|F_f(\boldsymbol{q})\right|^2}{q^4} \tag{1a}$$

$$= \left(\frac{2me^2}{\hbar^2}\right)^2 \frac{1}{k_i^2} \int \frac{\mathrm{d}q}{q^3} \, \mathrm{d}\phi \, \left|F_f(\boldsymbol{q})\right|^2 \tag{1b}$$

where the integral in (1*a*) is over the solid angle Ω subtended by the detector and e and m are the electronic charge and mass. In (1*b*) we have used (see figure 1)

$$\frac{k_f}{k_i}\,\mathrm{d}\Omega = \frac{k_f}{k_i}\sin\theta\,\mathrm{d}\theta\,\mathrm{d}\phi = \frac{1}{k_i^2} q\,\mathrm{d}q\,\mathrm{d}\phi$$

which follows from $\boldsymbol{q} = \boldsymbol{k}_i - \boldsymbol{k}_f$ [25].

In (1) $F_f(\boldsymbol{q})$ is the *form factor* for inelastic scattering from the ground state of the atom

into the final excited state:

$$F_f(\boldsymbol{q}) = \int \cdots \int \psi_f^* \psi_i \sum_{j=1}^{Z} \mathrm{e}^{\mathrm{i}\boldsymbol{q}\cdot\boldsymbol{r}_j}\, \mathrm{d}\boldsymbol{r}_1\, \mathrm{d}\boldsymbol{r}_2\, \cdots\, \mathrm{d}\boldsymbol{r}_Z$$
$$= Z \int \cdots \int \psi_f^* \psi_i \mathrm{e}^{\mathrm{i}\boldsymbol{q}\cdot\boldsymbol{r}_1}\, \mathrm{d}\boldsymbol{r}_1\, \mathrm{d}\boldsymbol{r}_2\, \cdots\, \mathrm{d}\boldsymbol{r}_Z$$

where $\psi_i(\boldsymbol{r}_1, \ldots, \boldsymbol{r}_Z)$ and $\psi_f(\boldsymbol{r}_1, \ldots, \boldsymbol{r}_Z)$ are the ground- and excited-state wavefunctions of the Z-electron atom. The second line follows from the antisymmetry of fermion wavefunctions. The many-electron wavefunctions appear as product wavefunctions with the initial and final states of the beam; hence the terms $\mathrm{e}^{\mathrm{i}\boldsymbol{q}\cdot\boldsymbol{r}_j}$ appear after the integration over the coordinate $\boldsymbol{r}$ of the plane-wave states has been done [25]. The final state of the atom is one in which an electron originally in an atomic core state has been excited to an unoccupied level. In the final state, the electrons relax to screen the core hole. We will want to account for this effect in our calculations.

Equation (1) has been derived by Bethe from the golden rule of Dirac and Fermi, and therefore implicitly assumes the first Born approximation for scattering, namely the first order in perturbation theory. Physically this means that incoming particles are scattered only once at each atomic site, producing just a single electronic excitation of the atom†. According to Bethe [25], the first Born approximation confines us to particle velocities greater than $(Z/137)c$ where c is the speed of light. An upper bound on the velocity is about $\frac{1}{2}c$ since the formula is non-relativistic. This strictly confines us to beam energies in EELS below 60 keV. However, relativistic corrections at modest velocities above $\frac{1}{2}c$ simply affect the prefactor in the differential cross section which is 'relativistically nearly correct' [25]. In our bandstructure calculations we include all relativistic effects except spin–orbit coupling; for simplicity, though, we will adhere to non-relativistic scattering formulae.

Bethe points out that if one were able to write the ground- and final-state atomic wavefunctions as single Slater determinants, then in $F_f(\boldsymbol{q})$ only one-electron integrals survive due to orthogonality of the one-electron orbitals; in other words the form factor reduces to a single important one-electron integral between core- and excited-electron orbitals. Thereby we make the one-electron approximation and write

$$F_{n\boldsymbol{k}}^{(1\mathrm{e})}(\boldsymbol{q}) = \int \mathrm{d}\boldsymbol{r}\; \varphi_{n\boldsymbol{k}}^*(\boldsymbol{r}) \mathrm{e}^{\mathrm{i}\boldsymbol{q}\cdot\boldsymbol{r}} \varphi_c(\boldsymbol{r}) = \langle n\boldsymbol{k}|\mathrm{e}^{\mathrm{i}\boldsymbol{q}\cdot\boldsymbol{r}}|c\rangle. \tag{2}$$

Here, $\varphi_c(\boldsymbol{r}) = \langle \boldsymbol{r}|c\rangle$ is the core-electron initial-state eigenfunction, having eigenvalue ε_c, and $\varphi_{n\boldsymbol{k}}(\boldsymbol{r}) = \langle \boldsymbol{r}|n\boldsymbol{k}\rangle$ is the final (band) state, with energy $\varepsilon_{n\boldsymbol{k}}$, which we have labelled with quantum numbers $\boldsymbol{k}$ and n, the wavevector and band index in the first Brillouin zone of the electronic states in a crystalline solid. By making the one-electron approximation and writing the final state as an unoccupied band state, we have made the transition from atomic to solid-state theory. In EELS we measure the intensity, or cross section, as a function of the energy loss E in the inelastic scattering caused by excitation of a core state‡. Therefore we shall replace σ_f in (1*b*) with a sum over all the cross sections $\sigma_{c,n\boldsymbol{k}}$ for excitations from the core state in question into final states with energy $\varepsilon_{n\boldsymbol{k}} = \varepsilon_c + E$. In this way, we define a differential cross section per unit energy for inelastic scattering with respect to energy loss E as

$$\sigma(E) = \sum_{n\boldsymbol{k}} \sigma_{c,n\boldsymbol{k}} \delta(\varepsilon - \varepsilon_{n\boldsymbol{k}}).$$

† This must not be confused with the notions of single and multiple scattering that are used as levels of approximation in solving the electronic structure problem in this context. In the bandstructure approach that we adopt here, multiple scattering in that sense is included up to all orders.

‡ We will use E $(=\hbar^2(k_f^2 - k_i^2)/2m)$ to denote the energy loss, and ε to denote energy relative to the energy zero defined in a bandstructure calculation, which we normally take to be the Fermi energy; hence in the one-electron bandstructure, $E = \varepsilon - \varepsilon_c$ where ε_c is the eigenvalue of the core state.

We should point out that the Dirac delta function appearing here is to weight the cross section according to the number of available states; the energy-conserving delta function in the usual statement of the golden rule is already worked out for the case of plane-wave states [24] and included in the prefactor in equation (1). Although in band theory all states have an infinite lifetime, it is a rather general result that states above the Fermi surface have a lifetime inversely proportional to the square of their energy relative to the Fermi level (at least in metals, and up to about 40 eV [26, 27]). Thus the delta function should be replaced by a Lorentzian function in order to be able to compare with experimental lineshapes. In our calculations we will simply apply a convolution to the density of states *post hoc*.

In an EELS experiment, the scattered beam is usually collected over a certain range of solid angle. Therefore what is measured is the number of electrons per unit time per unit energy $I(E)$ scattered with energy loss E; and if the incident flux of electrons is I_0 per unit area per unit time, after substituting (2) for $F_f(\boldsymbol{q})$ in (1*b*), the cross section proportional to $I(E)/I_0$ is

$$\sigma(E) = \left(\frac{2me^4}{\hbar^2}\right)\frac{1}{E_0}\int \frac{\mathrm{d}q}{q^3}\,\mathrm{d}\phi \sum_{n\boldsymbol{k}} |\langle n\boldsymbol{k}|\mathrm{e}^{\mathrm{i}\boldsymbol{q}\cdot\boldsymbol{r}}|c\rangle|^2\delta(\varepsilon - \varepsilon_{n\boldsymbol{k}}) \tag{3}$$

in which the integral is to be evaluated between $\boldsymbol{q}_{\min}$, the momentum transfer in forward scattering, and $\boldsymbol{q}_{\max}$ which is determined by the geometry of the apparatus (see figure 1). We have defined $E_0 = \hbar^2 k_i^2/2m$ as the energy of the incoming electron beam.

Equation (3) is the central result of the theoretical development; and can, in principle, be calculated to arbitrary precision within LDA once the exponential is expanded in powers of $\boldsymbol{q}\cdot\boldsymbol{r}$ [28]. However, to do the integration over q requires knowledge of the scattering conditions in the microscope and the orientation of the crystal. In what follows we will show that if the expansion of $\mathrm{e}^{\mathrm{i}\boldsymbol{q}\cdot\boldsymbol{r}}$ is taken to first order (the dipole approximation), then in the case of a cubic or isotropic material, the integration over q reduces to a constant prefactor multiplying the sum over $n\boldsymbol{k}$ in (3).

In the *dipole approximation* we write

$$\mathrm{e}^{\mathrm{i}\boldsymbol{q}\cdot\boldsymbol{r}} \approx 1 + \mathrm{i}\boldsymbol{q}\cdot\boldsymbol{r}$$

which can be only be fully justified by reference to experiment. The maximum value of r is the maximum extent of the core wavefunction, and the maximum value of q is determined by the collection angle in the microscope which is typically no greater than $\theta_{\max} = 20$ mrad. For carbide and nitride K edges we find thereby $\boldsymbol{q}\cdot\boldsymbol{r} \lesssim 1$. In the measurements by Pflüger *et al* [20, 22] the collection angle was ten times smaller; hence $\boldsymbol{q}\cdot\boldsymbol{r} \ll 1$ and agreement between our and their spectra indicates the validity of the dipole approximation. In addition, as we shall see (figure 8, below) and as has been found elsewhere [29], agreement between XANES and ELNES confirms its validity since in XAS the origin of the approximation is quite different [23]. Equation (1) also indicates that the cross section is dominated by small q. We return briefly to this question in section 8.

The matrix elements of unity will be zero due to orthogonality between core and band states, leaving only matrix elements of $\mathrm{i}\boldsymbol{q}\cdot\boldsymbol{r}$. Let us define, for brevity,

$$\langle z\rangle^2 = \sum_{n\boldsymbol{k}} |\langle n\boldsymbol{k}|z|c\rangle|^2\delta(\varepsilon - \varepsilon_{n\boldsymbol{k}}) \tag{4}$$

and similarly $\langle y\rangle^2$ and $\langle x\rangle^2$. By reference to figure 1(b), we may now evaluate the integral in (3) in the dipole approximation. Noting that

$$\cos^2\theta' = \left(\frac{k_f^2 - k_i^2 - q^2}{2k_i q}\right)^2$$

we have

$$\int \frac{\mathrm{d}q}{q^3}\,\mathrm{d}\phi\,\sum_{n\boldsymbol{k}}|\langle n\boldsymbol{k}|\boldsymbol{q}\cdot\boldsymbol{r}|c\rangle|^2\delta(\varepsilon-\varepsilon_{n\boldsymbol{k}}) = \int \frac{\mathrm{d}q}{q^3}\,\mathrm{d}\phi\,(q_x^2\langle x\rangle^2+q_y^2\langle y\rangle^2+q_z^2\langle z\rangle^2)$$
$$= \pi\ln\frac{q_{\max}}{q_{\min}}(\langle x\rangle^2+\langle y\rangle^2)+\pi A(2\langle z\rangle^2-\langle x\rangle^2-\langle y\rangle^2) \tag{5}$$

where

$$A=\frac{1}{8}\frac{2m}{\hbar^2}\frac{E^2}{E_0}\left(\frac{1}{q_{\min}^2}-\frac{1}{q_{\max}^2}\right)-\frac{1}{2}\frac{E}{E_0}\ln\frac{q_{\max}}{q_{\min}}+\frac{1}{8}\frac{\hbar^2}{2m}\frac{1}{E_0}(q_{\max}^2-q_{\min}^2).$$

Cross terms involving $q_xq_y, q_xq_z, \ldots$ need not appear in the first line of (5), since they vanish in the integral over ϕ. We can recast (5) into a transparent form using the experimental parameters θ_E and $\theta_{\max}$ [30]. To first order, we have $(k_i-k_f)/k_i = E/2E_0 \equiv \theta_E$ and therefore $q_{\min}^2 = k_i^2\theta_E^2$. To first order, $\boldsymbol{q}_{\min}$ is the component of $\boldsymbol{q}$ parallel to $\boldsymbol{k}_i$ and hence

$$q_{\max}^2 = k_i^2(\theta_{\max}^2+\theta_E^2).$$

Using these definitions, and retaining only the leading terms†,

$$\frac{1}{\pi}\int\frac{\mathrm{d}q}{q^3}\,\mathrm{d}\phi\,\sum_{n\boldsymbol{k}}|\langle n\boldsymbol{k}|\boldsymbol{q}\cdot\boldsymbol{r}|c\rangle|^2\delta(\varepsilon-\varepsilon_{n\boldsymbol{k}}) = \left(\ln\frac{\theta_{\max}}{\theta_E}-\frac{1}{2}\right)\left(\langle x\rangle^2+\langle y\rangle^2\right)+\langle z\rangle^2.$$

Equation (5) is the integral to evaluate in the dipole approximation in the general case of an anisotropic crystal, using a coordinate system for $\langle x\rangle^2$, $\langle y\rangle^2$ and $\langle z\rangle^2$ such that $-z$ is parallel to the beam direction. Normally this will involve taking linear combinations of $\langle x\rangle^2$, $\langle y\rangle^2$ and $\langle z\rangle^2$ calculated using conventional crystal axes. In the special case of specimen isotropy, the components of $\boldsymbol{r}$ (x, y and z) are equivalent by symmetry, and so we have $\langle x\rangle^2=\langle y\rangle^2=\langle z\rangle^2$. This will apply in randomly oriented polycrystalline samples and is exact for cubic crystals, but is an approximation for anisotropic single crystals. In the isotropic case our expression for the cross section (proportional to $I(E)/I_0$) reduces to

$$\sigma(E)=\left(\frac{4\pi me^4}{\hbar^2}\right)\frac{1}{E_0}\ln\frac{q_{\max}}{q_{\min}}\sum_{n\boldsymbol{k}}|\langle n\boldsymbol{k}|z|c\rangle|^2\delta(\varepsilon-\varepsilon_{n\boldsymbol{k}}).$$

Because of the weak logarithmic function, the intensity is essentially a constant times a weighted density of states. This follows once we recognize

$$\sum_{n\boldsymbol{k}}\delta(\varepsilon-\varepsilon_{n\boldsymbol{k}})$$

as an expression for the total density of states obtained from the energy bands $\varepsilon_{n\boldsymbol{k}}$ such as those in figure 2. A very important consequence of the dipole approximation is that *selection rules* require that if the core state has angular momentum ℓ then the final state must have angular momentum $\ell\pm1$. This comes about from the evaluation of the angular part of the integral (2) in the dipole approximation. If $\varphi_c(\boldsymbol{r})=\varphi_c(r)Y_{\ell m}$, $\varphi_{n\boldsymbol{k}}(\boldsymbol{r})=\varphi_{n\boldsymbol{k}}(r)Y_{\ell'm'}$, to evaluate (4) we write $z=\sqrt{4\pi/3}\,rY_{10}$, and get

$$\langle n\boldsymbol{k}|z|c\rangle=\sqrt{\frac{4\pi}{3}}\int\mathrm{d}r\;\varphi_{n\boldsymbol{k}}^*(r)r\varphi_c(r)\int\int\mathrm{d}\Omega\;Y_{\ell'm'}^*Y_{10}Y_{\ell m} \tag{6}$$

where the angular part is a Gaunt coefficient that is zero unless $\ell'=\ell\pm1$. Therefore, as Muller *et al* [12] have pointed out, the expression for the differential cross section resembles closely

† We assume $\theta_E \ll \theta_{\max} \ll 1$, which compares well with the conditions of our experiment in which $\theta_E\approx10^{-3}$, $\theta_{\max}\approx10^{-2}$. Incidentally, there is a solution of (5) for which the integral takes an average over $\langle x\rangle^2$, $\langle y\rangle^2$ and $\langle z\rangle^2$; namely when $\theta_{\max}/\theta_E=1.36$. Under these experimental conditions, therefore, the spectrum will be independent of crystal orientation.

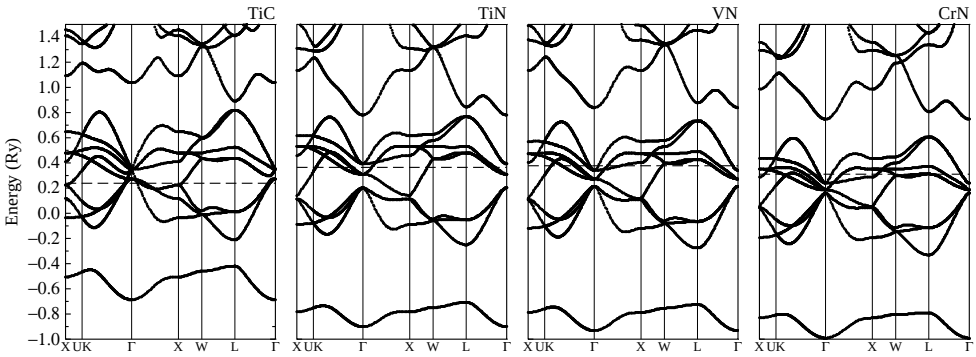

Figure 2. Energy bands of TiC, TiN, VN and CrN calculated in the local density approximation using the FP-LMTO method. These are the $\varepsilon_{n\boldsymbol{k}}$ appearing in equation (3), the energy as a function of wavevector $\boldsymbol{k}$ being plotted along high-symmetry lines in the Brillouin zone. The energy zero is the average Hartree potential in the interstitial region between the atomic spheres. The horizontal broken line shows the position of the Fermi level which separates occupied from unoccupied states. Bands around the Fermi level are bonding and antibonding combinations of anion 2p and cation 3d states which are strongly hybridized. The lowest band is the anion 2s band; bands above the pd manifold are mostly of anion 3d and cation 4s character.

a weighted (or *local*) density of states, such as a Mulliken projection onto basis functions with certain angular momentum centred at a particular atomic site. Thus one might reasonably replace the expression

$$\sum_{n\boldsymbol{k}} |\langle n\boldsymbol{k}|z|c\rangle|^2 \delta(\varepsilon - \varepsilon_{n\boldsymbol{k}}) \tag{7}$$

with a term proportional to q^{-2} times

$$\sum_{n\boldsymbol{k}} \left|F_{\text{proj}}(n\boldsymbol{k})\right|^2 \delta(\varepsilon - \varepsilon_{n\boldsymbol{k}}) \tag{8}$$

where

$$\left|F_{\text{proj}}\right|^2 = \sum_{\ell=-m}^{m} |\langle n\boldsymbol{k}|\boldsymbol{R}\ell m\rangle|^2 \tag{9}$$

and

$$\langle \boldsymbol{r}|\boldsymbol{R}\ell m\rangle = \chi_{\ell m}(\boldsymbol{r} - \boldsymbol{R})$$

is one of the basis functions in which the band states are being expanded, having the correct angular momentum to satisfy the dipole selection rules and centred on the atomic site $\boldsymbol{R}$ in question. For example figure 3 shows projected densities (8) obtained from the energy bands in figure 2. This should be a reasonable approach for any matrix element F_{proj} that projects out the correct angular momentum according to the dipole selection rule, as long as the energy dependence of the radial part of the integral (6) is very weak. Muller *et al* [12] have calculated this energy dependence for the case of Ni–Al alloys. A central goal of the present work is to compare spectra obtained from the two weighted densities of states, equations (7) and (8).

4. The edge threshold

The absorption edge occurs when the beam has enough energy to excite a particular atomic core electron into the lowest unoccupied state, which in a metal is at the Fermi energy. In

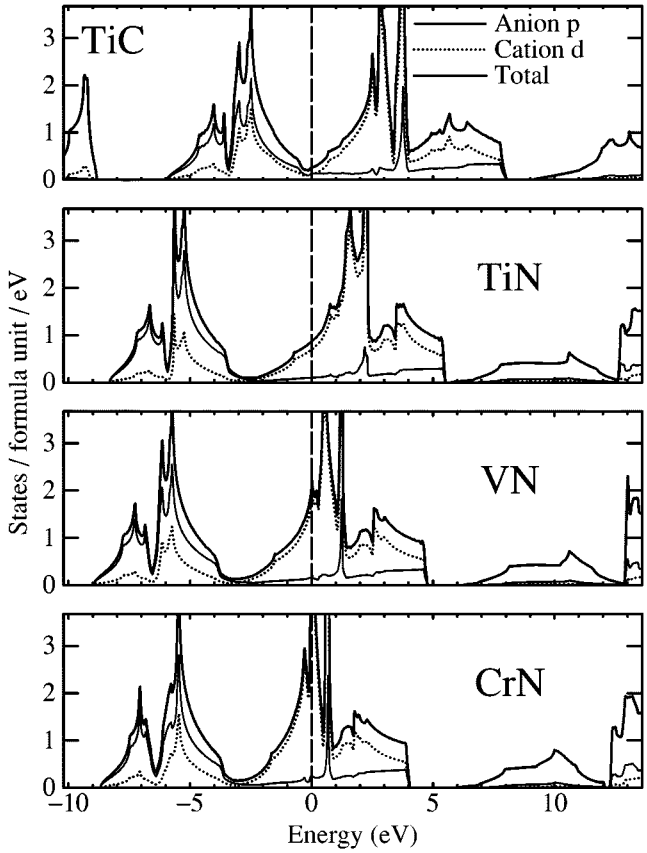

Figure 3. Total and Mulliken projected densities of states in TiC, TiN, VN and non-magnetic CrN, derived from the energy bands in figure 2. Here we have moved the energy zero to coincide with the Fermi level, and used eV as units of energy. The deep minimum, which is near the Fermi level in TiC, in all figures separates the bonding and antibonding states.

the one-electron approximation one takes this threshold energy $E_{\rm th}$ to be the Fermi energy measured relative to the eigenvalue of the core electron. However, the eigenvalue of the core state depends on its occupancy such that, in density functional theory, its eigenvalue is given according to Janak's theorem by [31, 32]

$$\varepsilon_c(q_c) = \frac{\partial E_{\rm HK}}{\partial q_c}$$

where $E_{\rm HK}$ is the Hohenberg–Kohn (HK) total energy and q_c is the number of electrons occupying the core state.

The proper way to calculate $E_{\rm th}$ is as the difference between two HK total energies: the ground-state energy and the energy of the state in which there is a core hole with the missing electron occupying the lowest unoccupied level of the ground-state system. Both should be self-consistently calculated to allow the electronic system to respond to the presence of the core hole. Thus, if $E_{\rm HK}(q_c)$ is the HK total energy,

$$E_{\rm th} = E_{\rm HK}(q_c)\big|_{q_c=1} - E_{\rm HK}(q_c)\big|_{q_c=2} \tag{10}$$

is an exact expression within density functional theory. This is called the ΔSCF approach [15] since it involves the energy difference between two self-consistent fields. If $\varepsilon_c(q_c)$ is *linear* in

q_c (say, $\varepsilon_c(q_c) = \varepsilon_c(0) + U_c q_c$) then according to Slater's transition state theory [15, 32]

$$E_{\rm th} = \int_2^1 \frac{\partial E_{\rm HK}}{\partial q_c}\,{\rm d}q_c = \int_2^1 [\varepsilon_c(0) + U_c q_c]\,{\rm d}q_c = -\varepsilon_c(q_c)\big|_{q_c=3/2}. \tag{11}$$

This means we can either calculate $E_{\rm th}$ as $E_{\rm HK}(1) - E_{\rm HK}(2)$ or as the Fermi energy relative to the core eigenvalue in a self-consistent calculation in which there is *half* a core hole. One can think of the integral as representing a thought experiment in which the eigenvalue of the core level is continuously measured as the core occupancy is slowly varied between two and one (i.e., as the core hole 'grows'). The point is that, employed as a one-electron theory, the LDA eigenvalues do not correspond to excitation energies of the system, although they are often interpreted as such. However, if the calculation is done so as to allow electronic relaxation as in equations (10) and (11), then the LDA does a good job of describing the screening. In other words, the LDA one-electron levels are in error, but the Coulomb repulsion

$$U_c = \frac{\partial^2 E_{\rm HK}}{\partial q_c^2}$$

is nearly correctly rendered in a self-consistent LDA calculation. We can then regard the energy levels strictly as excitation energies *if* they are calculated self-consistently in the presence of half a hole in the core state which is excited.

We can test this by calculating $E_{\rm th}$ in these three different approximations and comparing to experiment. We show data in table 1 for a wide range of transition metal carbides and nitrides. A fuller comparison of experiment and theory for these compounds will appear elsewhere [33]. As discussed in section 2.2, we have taken the experimental thresholds from our earlier work [16,17] but take those of Pflüger *et al* [20,22] when their values differ from ours. Our theoretical results are essentially in accord with those of Aryasetiawan and Gunnarsson for the semi-core levels in semiconductors [34]. The one-electron approximation underbinds the core levels by about 20 eV. The Slater transition state approximation is in excellent agreement with the ΔSCF approach, indicating that ε_c is indeed linear in q_c. However, the LDA in the ΔSCF approach introduces an error of about 4 eV into the threshold energies. Aryasetiawan and Gunnarsson did calculations beyond LDA (using the GW approach) to investigate how this remaining error can be removed; we have not done this. The power of the transition state theory is that when we come to calculate the spectrum at the near edge, we can maintain half of a core hole in order to account for the screening effects missing in the one-electron approximation. These are sometimes called 'final-state effects'. This approach has also recently been adopted by Köstlmeier and Elsässer in the context of the pseudopotential approximation for Mg and Al oxides [35].

A significant difference between the one-electron and transition state results is that in the one-electron approximation, the mean value of the underbinding of the N K edges in the calculation is 3.25 eV greater than that of the C K edges, whereas in the transition state approximation the mean overbinding of the N K edges is only 0.55 eV more than that of the C K edges. So, whereas the transition state theory corrects all but about 4 eV of the one-electron error, the remaining discrepancy with experiment is very much the same for both nitride and carbide anions, namely 4.22 ± 0.44 eV of overbinding in the calculations. As we will see below, this provides us with a prescription for calculating *absolute values* in the electron energy-loss spectrum.

The screening of the core hole turns out to be so short ranged that $E_{\rm th}$ calculated in larger supercells with just a central atom having the core hole is identical (to within 0.2 eV) to that from a single unit cell which mimics a crystal containing a core hole in every anion. The supercell approach is the correct one: in a typical EELS experiment, the electron flux I_0 is

about one electron per nm^2 per 10^{-10} s, whereas a typical electronic relaxation time (based on the plasmon energy) is about 10^{-16} s.

Finally, we should remark that invoking well known generalized gradient approximations was found to make no real improvement over the LDA. On the contrary, using two separate gradient corrections [36, 37] we found that the one-electron threshold energies were closer to experiment by about 3 eV. But the ΔSCF and transition state values overcorrect the experiment, so the final error, when including gradient corrections, was about 3 eV greater than in the LDA.

5. Electronic structure

In the results shown in table 1, and in all that follows, we have solved the Kohn–Sham density functional equations using full-potential (FP) LMTO-based methods [38]. The benefits of such all-electron methods is that the core states are allowed to relax during self-consistency providing greater accuracy in the matrix element evaluations than in, say, pseudopotential methods [2, 35]. Furthermore, all relativistic effects except spin–orbit coupling are included in the relaxation of the valence- and core-electron wavefunctions. We have adopted two FP-LMTO schemes. We use a method due to Methfessel [39, 40] which uses a conventional Hankel function basis and which thereby allows a rather transparent Mulliken projection onto atomic-like basis functions for evaluating F_{proj}, equation (9); and a newer scheme of Methfessel and van Schilfgaarde [41], which uses a basis of smooth Hankel functions, in which we have implemented the calculation of the dipole matrix elements in (7).

We begin by showing the electronic bandstructure of the four transition metal compounds in figure 2. The energy bands are displayed, as is conventional, in atomic Rydberg units of energy (1 Ryd $=$ 13.61 eV) with an energy zero which is the average Hartree potential in the interstitial region of the crystal. Points of high symmetry are labelled with the usual symbols [42]. The energy bands show clear similarities which are emphasized further by the densities of states shown in figure 3. The energy zero is now shifted to coincide with the Fermi energy, and we use eV as units of energy to be consistent with spectroscopic usage. In each compound the anion (C or N) 2s band is isolated below a manifold of anion 2p and cation (Ti, V, Cr) 3d states which are hybridized to form bonding and antibonding combinations. The anion 2s band can be seen at the low-energy end of the TiC figure but is below the minimum energy of the figures for the other compounds. In TiC, which is the strongest of the 'hard metals', the bonding states are filled and separated by a minimum in the density of states from the unoccupied antibonding states; and this is the origin of this material's mechanical and thermodynamic stability. Essentially this is because bonding states are lower in energy than the free-atom states from which they are derived, and conversely the antibonding states are higher. Therefore, the more bonding states are filled, the greater the cohesion in forming the solid; and the more antibonding states are filled, the weaker the cohesion. Above the pd manifold, separated by a band gap, are the higher-lying bands, mostly of cation 4s and anion 3d character. What is striking is that the electronic structure of the remaining compounds is well approximated by that of TiC, with the Fermi level raised by the addition of electrons due to increasing the atomic number of either the anion or cation. This argues that a simple, empirical tight-binding approach to the electronic structure of carbide and nitride transition metal binary and ternary (and higher) alloys is likely to be successful. This picture breaks down somewhat with CrN where there is significant band narrowing as well as magnetic instability, as we shall see below.

6. The anion K edge of TiC, TiN and VN

Within the LMTO method we can calculate the dipole matrix elements in (6) as long as the core state has s symmetry (i.e., $\ell = 0$). This avoids the question of multiplet structure which cannot be tackled in the conventional solid-state LDA [1, 43, 44]. It is clear from figure 3 that unoccupied states of $\ell = 1$ character are the p-projected local density of states at the anion sites. Therefore we may calculate the near-edge structure at the anion K edge as either equation (7): the density of states weighted at each $\boldsymbol{k}$-point by the (squared) dipole matrix element (6); or as equation (8) with the sum in equation (9) being over all LMTO basis functions $\chi_{\ell m}(\boldsymbol{r})$ centred on anion sites with angular momentum $\ell = 1$†.

As mentioned earlier, in order to compare lineshapes with experiment we need to account for the finite lifetime of initial and final states. To do this we follow procedures of Müller *et al* [11] and Muller *et al* [12] and convolute the density of states with a Lorentzian of width

$$\Gamma = \Gamma_i + \Gamma_f .$$

Here Γ_i is the width of the core state, which can be obtained from atomic data [45], and Γ_f is the width of the final state. A general procedure would be to have $\Gamma_f \propto (\varepsilon - \varepsilon_F)^2$, where ε_F is the Fermi energy, and fit the proportionality constant to, say, the linewidth of the second or third peak. However, Muller *et al* use an expression for jellium, namely [26]

$$\Gamma_f = \frac{\pi^2\sqrt{3}}{128} E_p \left(\frac{\varepsilon - \varepsilon_F}{\varepsilon_F - \varepsilon_0} \right)^2$$

in which E_p is the plasmon energy and $\varepsilon_F - \varepsilon_0$ is the width of the occupied part of the band. By using plasmon energies taken from the low-loss region of the EELS spectra and using the bottom of the anion s band for ε_0 we obtain very good agreement for the linewidths as seen below. The spectra are finally convoluted with a 0.4 eV wide Gaussian to account for the instrumental resolution.

Figures 4, 5 and 6 show the experimental ELNES for TiC, TiN and VN compared to three calculated spectra. We have arbitrarily scaled the calculations so that the intensity approximately matches the experimental intensity near the first peak. A prescription for predicting absolute intensity has been described by Muller *et al* [12]; it involves aligning the intensity calculated at energies above the fine structure to the decaying atomic intensity [5, 6]. But the high-energy density of states is not available to the linear bandstructure methods we use here. In order to correct for the LDA error in the threshold energy, we have subtracted the mean value for all anions, namely 4.22 eV, from the transition state values in table 1 when aligning the spectra on the energy axis. This provides an absolute prediction of the energy loss with a single many-electron correction to the LDA obtained by comparing with experiment. We show the total density of states projected onto the anion p LMTOs, equation (8); the one-electron approximation to the density of states weighted with the dipole matrix element, equation (7); and the same quantity calculated in a unit cell in which each anion has half a core hole in the 1s state. In each case the near-edge structure shows two characteristic peaks which can be identified with the peak in the partial p density of states followed by the drop at the upper band edge. The band gap above the pd manifold is seen as a deep minimum in the near-edge structure. The position of this minimum measures the *width* of the unoccupied part of the pd manifold, the agreement between theory and experiment being very good, despite the fact that the LDA usually overestimates the width of bands derived from transition metal d electrons [46].

† In fact in each ℓm channel we use three LMTOs having different localization energies [40].

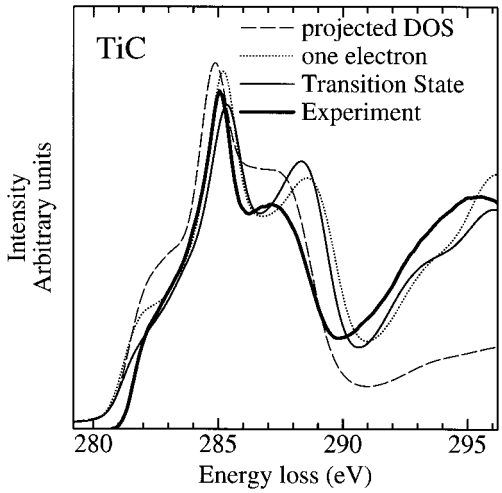

Figure 4. The experimental anion K-edge ELNES in TiC superimposed on our three theoretical estimates of the spectra: the Mulliken projected anion 2p density of states, equation (8); the density of states weighted with the dipole matrix element, equation (7); and the same quantity calculated self-consistently in the presence of half a core hole in the anion 1s state: the Slater transition state approximation.

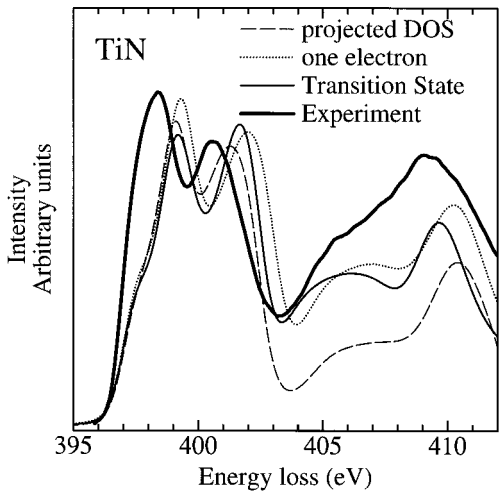

Figure 5. As figure 4, but for TiN.

Overall, the agreement between the experiment and the calculations is very good. Considering the calculations first, the regions up to the first main peak match very well. The energy of the second peak is generally lowest in the projected density of states and highest in the one-electron dipole matrix element with the value for the transition state matrix element falling between these extremes. The energies of the deep minima ∼10 eV above the threshold agree to better than 1 eV as do those of the higher-energy features, The effect of omitting the energy dependence of the matrix element (see the discussion following equation (9)) in the projected density of states shows up clearly in these high-energy features which appear with

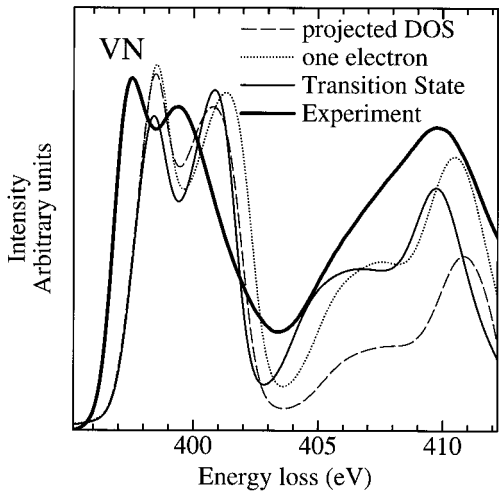

Figure 6. As figure 4, but for VN.

much lower intensity when using the Mulliken density compared with the calculation of the dipole matrix element.

Turning to the experimental data, the absolute alignment of the TiC spectrum with the calculations is excellent because they show a common step at the threshold, and this is sufficiently far from the sharp peak in the unbroadened partial density of states, shown in figure 3, that the determination of the experimental threshold is unambiguous. The agreement for TiN is good, but the low-energy shoulder at the threshold in the calculation is not visible in the experimental data. In the case of VN, the agreement of the absolute threshold is less good and the experimental width of the unoccupied pd manifold is, if anything, wider than that in the calculation. There is a difference of 0.47 eV between the Slater transition state threshold and the experimental threshold of Pflüger *et al* [20]. There is an even bigger difference if our experimental value is used [16]. We should mention here that from the experimental spectra, we obtain the threshold as the point of maximum slope behind the first peak; and in figures 5 and 6 especially, we see that the threshold in the calculations does not correspond to the criterion of maximum slope. This is a further source of discrepancy between the experimental and calculated values of the threshold energies and serves to emphasize the difficulties in determining the values of the threshold energy experimentally.

7. The anion K edge of CrN

We found that the two-peak structure was not observed in CrN; rather a single peak was seen which is not consistent with the partial anion density of states in figure 3. In that figure, we see a narrowing of the band and a large density of states at the Fermi level. Added to a large Stoner parameter in Cr (≈50 mRyd—nearly 5 mRyd larger than in V or Ti [47]), this leads one to expect to see a magnetic instability [48]. We have used local spin-density functional theory (LSDA), with collinear moments, to calculate the electronic structure and magnetic energy in ferromagnetic (FM) CrN and antiferromagnetic (AFM) CrN in the structure reported by Corliss *et al* [49], having a Néel temperature of $T_N = 288$ K [50]. In this structure, pairs of (220) Cr planes of the rock-salt structure have spins aligned ferromagnetically in the (220)

plane; but the pairs of planes themselves are stacked in antiferromagnetic alignment along the [110] direction. This magnetic structure lowers the symmetry to orthorhombic, which allows the lattice constants and internal coordinates degrees of freedom to relax. However, this lattice distortion occurs only below the Néel temperature which is below room temperature; as noted in section 2.1, our specimen showed a cubic diffraction pattern at room temperature.

Ferromagnetic CrN is 16 mRyd (217 meV) per CrN formula unit lower in energy than the non-magnetic (NM) phase. The magnetic moment is $2.18\mu_B$ per CrN formula unit. Figure 7 shows the Mulliken projected densities of states for the Cr 3d and N 2p LMTO channels. This is a very clear example of rigid-band itinerant magnetism with an exchange splitting of about 0.1 Ryd (1.3 eV). Because of covalency and because each N atom is surrounded by six Cr atoms with the same orientation of the magnetic moment, the N 2p states are also exchange split, by the same amount. In fact one sees in figure 7 that the exchange splitting is not uniform within the band, being rather less in the bonding manifold. The exchange splitting leaves a peak in the majority-spin density of states at the Fermi level, and this may be why this is not the lowest-energy magnetic state.

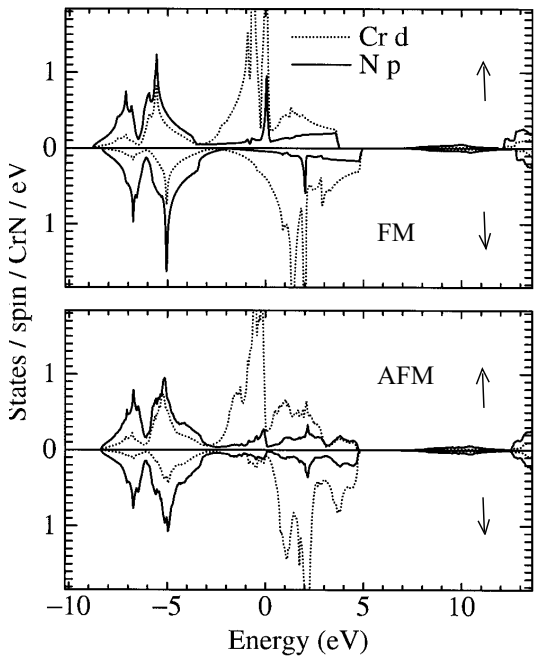

Figure 7. The Mulliken projected N 2p and Cr 3d densities of states in FM and AFM CrN. Panels show up- and down-spin-projected densities. In the AFM structure the roles of up and down are reversed in alternating pairs of (220) planes of Cr in the rock-salt structure.

Antiferromagnetic CrN is 25 mRyd (336 meV) per CrN formula unit lower in energy than the non-magnetic phase. (We find that this is 1 mRyd lower than the MnO AFM structure, which is AFM in the [111] direction; furthermore, relaxation of the lattice constants into those given by Corliss *et al* lowers the energy by a further 3 mRyd.) The local Cr magnetic moment is about $2.00\mu_B$. This is less than in FM CrN, but the local moments on the Cr atoms are about the same. The lower total moment can be understood from figure 7 which shows that only the Cr 3d bands are exchange split. The splitting is less uniform than in FM CrN, being zero at the top and bottom of the pd manifold. Each N atom has four spin-up and two spin-

down Cr neighbours; the spin polarization of the anions is frustrated and amounts to zero. There is now a deep minimum in the density of states at the Fermi level and the bonding is strongly covalent in the manifold of bonding states. This is a rare case of a magnetic covalent compound.

In figure 8, we compare the experimental ELNES and XANES spectra with N 2p projected densities as in figure 7, broadened according to the prescription described earlier. We have not calculated absolute energy loss here; instead we have lined up the spectra and densities of states by eye. The excellent agreement between the two experiments argues strongly in favour of the dipole approximation. A slight difference between the two spectra is a shoulder in the XANES at about 4 eV, which is less prominent in the ELNES. The NM CrN theoretical spectrum gives the same two-peak structure as TiC, TiN and VN and is not consistent with the experimental data. The AFM calculation is in better agreement with the experimental spectra. It predicts a feature on the high-energy side of the first peak which is seen in the XANES and less prominently in the ELNES. The AFM calculation also shows similar features in the 5–15 eV energy range but at lower intensity; we recall that this is consistent with our neglect of the energy dependence of the matrix element, since we are using Mulliken densities to predict near-edge structure here. Both the NM and FM calculations show totally different structure in this energy range.

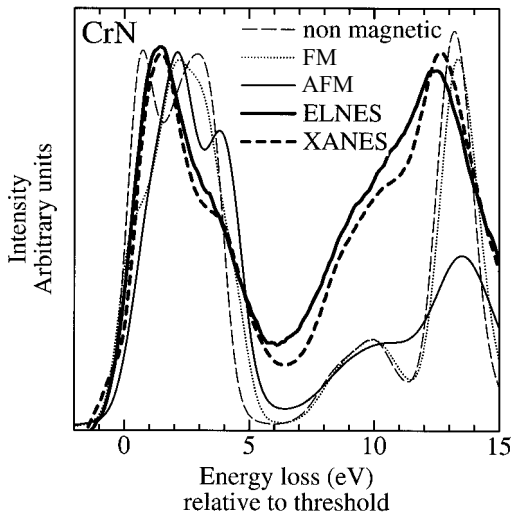

Figure 8. The experimental anion K-edge ELNES and XANES in CrN compared with the Mulliken projected N 2p densities of states in NM, FM and AFM magnetic structures.

Ferromagnetic CrN has not been observed as far as we are aware, and this result is consistent with our total-energy calculations. Because of the large magnetic energy we would expect local moments to persist right up to temperatures of $kT \approx 200$ meV, namely $\sim$2000 °C. We also do not expect the FM phase to occur even in the strongest possible magnetic fields. As mentioned in section 2.2, we have found no detectable changes in N K-edge structure between −140 °C and +160 °C. This suggests that, given that long-range order vanishes within that range of temperature, the ELNES is dominated by the first few moments of the density of states.

8. Discussion

On the whole the agreement between theory and experiment is very good on the scale of electron volts in the near-edge structure. It is clear that a Mulliken projection onto unoccupied states whose symmetry honours the dipole selection rule is a good substitute for the actual dipole matrix element. A number of authors [2, 51] have proposed writing (from (1*a*) with $k_f/k_i \approx 1$)

$$\frac{\mathrm{d}\sigma(E)}{\mathrm{d}\Omega} = \left(\frac{2me^2}{\hbar^2}\right)^2 \frac{1}{q^2} \left\{ |m_{\ell+1}|^2 \, \rho_{\ell+1}(\varepsilon) + |m_{\ell-1}|^2 \, \rho_{\ell-1}(\varepsilon) \right\} \tag{12}$$

for a core state of angular momentum ℓ. Here, the m_ℓ are energy-dependent matrix elements—the radial part of the integral in equation (6)—and $\rho_\ell(\varepsilon)$ are projected densities of states of angular momentum ℓ. As Muller *et al* [12] and Nelhiebel *et al* [28] point out, equation (12) does not follow from the formal theory or from the definition of Mulliken projected DOS. However, equation (12) is rigorously correct in the LAPW formalism if the ℓ-projected densities of states are obtained by a projection, as in (9), onto atom-centred spherical harmonics rather than basis functions [11], i.e., replace $\langle \boldsymbol{r}|\boldsymbol{R}\ell m\rangle$ with $Y_{\ell m}(\boldsymbol{r}-\boldsymbol{R})$ in (9). The difficulty with such a projection is that, except in the case of the atomic spheres approximation used in [11], the projection does not conserve the total number of states. From our point of view it is also of less physical interest than a Mulliken projection, since if the Mulliken projection turns out to be of value (as it does here) then this has much wider implications, for example as an approximate scheme for EELS and XANES predictions in LCAO and tight-binding models.

By directly calculating the dipole matrix elements one avoids approximations such as the dependence of the result on the choice of basis functions. There remains the approximation of a dipole matrix element. This can easily be removed in the present context by including quadrupole terms (and higher if needed) [28]. However, this is at the expense of the integration over q in equation (3). This is not difficult to do, but one would need to know the orientation of the crystal with respect to the beam, as one would indeed in the dipole approximation if the crystal were not cubic or isotropic. Our approach differs from that of Nelhiebel *et al* [28] who obtain the intensity as a function of $\boldsymbol{q}$. This approach is valuable if one is measuring the $\boldsymbol{q}$-dependence of the scattering as opposed to measuring the scattering integrated over a range of $\boldsymbol{q}$, as here. On the other hand the popular approach based on equation (12), and our Mulliken approach, neglects the $\boldsymbol{q}$-dependence and furthermore assumes an isotropic specimen. In deriving equation (5) we have shown how to predict the EELS intensity in the usual experimental arrangement. We see, incidentally, that referred to the coordinate system of figure 1 one cannot distinguish experimentally between $\langle x\rangle^2$ and $\langle y\rangle^2$ without either changing the crystal orientation relative to the incident direction or biasing the range of $\boldsymbol{q}$ collected by misaligning the collection aperture with respect to the incident direction.

We have already remarked that the rigid-band picture seems very much applicable to the compounds we have studied here, and this leads one to suppose that a working tight-binding model could be constructed to explore questions of non-stoichiometry and ternary alloying in the hard metals. Because of the near equivalence of the dipole matrix element to an appropriate partial density of states, it is probable that the tight-binding model could even be used to predict the near-edge structure in complex alloys.

We next remark upon the Slater transition state approach to what are sometimes called 'final-state effects', or removing the 'sudden approximation' [35]. For the calculation of the threshold energy this has a large effect and the self-consistent LDA approximation to U_c leaves us with a remaining error of a few eV for E_{th}. Clearly there is a large electronic relaxation involved in screening the core hole, but this is accomplished primarily by core-level shifts and

a downward shift of the anion 2s band; the unoccupied band states are little affected by the presence of the core hole. We can see this in the theoretical spectra in figures 4, 5 and 6 in which peaks above the threshold are pulled down in energy by only $\sim$1 eV as a result of the electronic relaxation.

It is gratifying that in the long run a simple Mulliken-like projection is adequate to describe the near-edge structure, as indeed is predicted by equation (12). In fact we have exploited this to simplify our calculations for the magnetic phases of CrN. Even at this level of approximation we can clearly distinguish between different magnetic states in LSDA and compare with experimental spectra. This exposes nicely the connection between ELNES and XANES and the LSDA as probes of magnetic structure in solids. In the case of CrN the magnetism is too strong to observe any changes in electronic structure near the transition temperature. However, this does not rule out the possibility in weakly magnetic crystals of studying fluctuations in local moments. The most modern bandstructure approaches now include non-collinear magnetism and finite-temperature spin dynamics [52]. The time-averaged Mulliken density may be easily calculated as a natural by-product of the dynamical simulations.

9. Conclusions

We are able to predict the electron energy loss and x-ray absorption near-edge structure subject to the following essential approximations being made.

(1) The first Born approximation.
(2) The one-electron approximation for matrix elements.
(3) The local density approximation for exchange and correlation.
(4) Slater transition state theory to account for electronic relaxation to screen the core hole.

The validity of these has been discussed in the text. The most serious is the one-electron approximation. This confines us in particular to a discussion of K edges, since the usual LDA, with its neglect of orbital-dependent exchange, does not adequately deal with multiplet splitting.

As many authors have surmised, one can predict the dipole-allowed transition cross sections in ELNES and XANES using a simple angular momentum projection of the density of states. This has a bearing on simpler electronic structure models such as the tight-binding approximation. When one includes the screening of the core hole, even at only the LDA level, this greatly affects the threshold energies and brings them into agreement with experiment, with a residual error of a few eV. The electronic relaxation of the core hole affects the unoccupied levels to a lesser extent: typically there are downward shifts of 1–2 eV.

Our study of CrN has revealed the interesting and significant fact that the *anion* near-K-edge structure can be used to probe the *cation* spin alignments. We do not find any temperature dependence of the ELNES due to the large magnetic energy in CrN. However, in weakly magnetic materials we see ELNES and XANES as providing techniques to investigate complex, non-collinear magnetic structures. This could in future be coupled with the recent development of spin dynamics [52] in the LSDA to further refine the connections between experimental and theoretical approaches to magnetic structure and its temperature dependence.

Acknowledgments

ATP wishes to thank Dr Sibylle Köstlmeier, Dr Christian Elsässer and Dr Tchavdar Todorov for valuable discussions. We are grateful to Dr C G Chatfield for supplying the TiC sample;

Professor G C Weatherley for the TiN sample; Professor W Lengauer for the VN sample; Dr I P Parkin, Mr A Nartowski and Ms F Docherty for the XRD analysis; Dr I W Kirkman for help in operating beam line 1.1 at the Daresbury Laboratory; and Mr J Gallagher for preparing the CrN specimen for XAS. The EPSRC provided support under grants GR/K93600, GR/L66953 and GR/L08427.

References

[1] de Groot F M F 1994 *J. Electron Spectrosc. Relat. Phenom.* **67** 529
[2] Rez P, Bruley J, Brohan P, Payne M and Garvie L A J 1995 *Ultramicroscopy* **59** 159
[3] Ankudinov A L, Ravel B, Rehr J J and Conradson S D 1998 *Phys. Rev.* B **58** 7565
[4] Lee P A and Pendry J B 1975 *Phys. Rev.* B **11** 2795
[5] Manson T and Cooper J W 1968 *Phys. Rev.* **165** 126
[6] Leapman R D, Rez P and Mayers D F 1980 *J. Chem. Phys.* **72** 1232
[7] Ducastelle F and Cyrot-Lackmann F 1970 *J. Phys. Chem. Solids* **31** 1295
Ducastelle F and Cyrot-Lackmann F 1971 *J. Phys. Chem. Solids* **32** 285
Haydock R, Heine V and Kelly M J 1972 *J. Phys. C: Solid State Phys.* **5** 2845
[8] Weng Xudong and Rez P 1989 *Phys. Rev.* B **39** 7405
[9] Lindner Th, Sauer H, Engel W and Kambe K 1986 *Phys. Rev.* B **33** 22
[10] Wu Z Y, Ouvrard G, Gressier P and Natoli C R 1997 *Phys. Rev.* B **55** 10 382
[11] Müller J E and Wilkins J W 1984 *Phys. Rev.* B **29** 4331
[12] Muller D A, Singh J and Silcox J 1998 *Phys. Rev.* B **57** 8181
[13] Muller D A, Batson P E, Subramanian S, Sass S L and Silcox J 1994 *Mater. Res. Soc. Symp. Proc.* **319** 299
[14] Hohenberg P and Kohn W 1964 *Phys. Rev.* **136** B864
Kohn W and Sham L 1965 *Phys. Rev.* **140** A1133
[15] Jones R O and Gunnarsson O 1989 *Rev. Mod. Phys.* **61** 689
[16] Craven A J 1995 *J. Microsc.* **180** 250
[17] Craven A J and Garvie L A J 1995 *Microsc. Micranal. Microstruct.* **6** 89
[18] Goldschmidt H J 1967 *Interstitial Alloys* (Oxford: Butterworths) chs 3 and 4
[19] Lengauer W and Ettmayer P 1985 *J. Less-Common Met.* **109** 351
[20] Pflüger J, Fink J, Crecelius G, Bohnen K P and Winter H 1982 *Solid State Commun.* **44** 489
[21] Craven A J and Buggy T W 1981 *Ultramicroscopy* **7** 27
[22] Pflüger J, Fink J and Schwartz K 1985 *Solid State Commun.* **55** 675
[23] Desjonquères M C and Spanjaard D 1996 *Concepts in Surface Physics* (Berlin: Springer) appendix F
[24] Roman P 1965 *Advanced Quantum Theory* (New York: Addison-Wesley)
[25] Bethe H A 1964 *Intermediate Quantum Mechanics* 1st edn (New York: Benjamin) ch 15
[26] Pines D and Nozières P 1966 *Normal Fermi Liquids (The Theory of Quantum Liquids vol I)* (New York: Benjamin) pp 61, 308
[27] Mahan G D 1990 *Many-Particle Physics* 2nd edn (New York: Plenum) p 488
[28] Nelhiebel M, Louf P-H, Schattschneider P, Blaha P, Schwartz K and Jouffrey B 1999 *Phys. Rev.* B **59** 12 807
[29] Vlachos D *et al* 2000 to be published
[30] Egerton R F 1986 *Electron Energy Loss Spectroscopy in the Electron Microscope* (New York: Plenum) p 147
[31] Janak J F 1978 *Phys. Rev.* B **18** 7165
[32] Parr R G and Yang W 1989 *Density Functional Theory of Atoms and Molecules* (Oxford: Oxford University Press)
[33] Scott A J *et al* 2000 to be published
[34] Aryasetiawan F and Gunnarsson O 1996 *Phys. Rev.* B **54** 17 564
[35] Köstlmeier S and Elsässer C 2000 *Phys. Rev.* B at press
[36] Perdew J P, Burke K and Wang Y 1996 *Phys. Rev.* B **54** 16 533
[37] Perdew J P, Burke K and Ernzerhof M 1996 *Phys. Rev. Lett.* **77** 3865
[38] Andersen O K, Methfessel M, Rodriguez C O, Blöchl P and Polatoglou H M 1989 *Atomistic Simulation of Materials: Beyond Pair Potentials* ed V Vitek and D J Srolovitz (New York: Plenum) p 1 and references therein
[39] Methfessel M 1988 *Phys. Rev.* B **38** 1537
[40] Rodriguez C O, Methfessel M and Andersen O K 1989 *Phys. Rev.* B **40** 2009
Paxton A T, Methfessel M and Polatoglou H M 1990 *Phys. Rev.* B **41** 8127

[41] Methfessel M and van Schilfgaarde M 1997 *NFP Manual 1.01* (Frankfurt/Oder: IHP) obtainable by electronic mail from methfessel@ihp-ffo.de
[42] Jones H 1960 *The Theory of Brillouin Zones and Electronic States in Crystals* (Amsterdam: North-Holland)
[43] von Barth U 1979 *Phys. Rev.* A **20** 1693
[44] Gunnarsson O and Jones R O 1980 *J. Chem. Phys.* **72** 5357
[45] Keski-Rahonen O and Krause M O 1974 *At. Data Nucl. Data Tables* **14** 139
[46] Aryasetiawan F and Gunnarsson O 1998 *Rep. Prog. Phys.* **61** 237
[47] Janak J F 1977 *Phys. Rev.* B **16** 255
[48] Andersen O K, Madsen J, Poulsen U K, Jepsen O and Kollar J 1977 *Physica* B **86–88** 249
Christensen N E, Gunnarsson O, Jepsen O and Andersen O K 1988 *J. Physique Coll.* **49** C8 17
[49] Corliss L M, Elliot N and Hastings J M 1960 *Phys. Rev.* **117** 929
[50] Lacour-Gayet P, Ducastelle F and Costa P 1973 *J. Physique* **34** 1001
[51] Rez P, Weng Xudong and Ma Hong 1991 *Microsc. Microanal. Microstruct.* **2** 143
[52] Antropov V P, Katsnelson M I, van Schilfgaarde M and Harmon B N 1995 *Phys. Rev. Lett.* **75** 729
Antropov V P, Katsnelson M I, Harmon B N, van Schilfgaarde M and Kusnezov D 1996 *Phys. Rev.* B **54** 1019